Colloids and Surfaces B: Biointerfaces 238 (2024) 113877

Contents lists available at ScienceDirect

Colloids and Surfaces B: Biointerfaces

journal homepage: www.elsevier.com/locate/colsurfb

Development of a precision tumor bone metastasis model by a magnetic micro-living-motor system

Jialu Zhang [a], Zhengyuan Wang [a], Dingyi Zhang [a], Qiyan Chen [a], Jiawei Xu [b], Luxia Tang [b], Jinyan Luo [b], Qiusui Mai [c], Xia Lu [b], Leyi Tan [b], Ning Gan [d,*], Qianli Jiang [a,e,**]

[a] Department of Haematology, Nanfang Hospital, Southern Medical University, Guangzhou, China
[b] School of the first Clinical Medicine, Southern Medical University, Guangzhou, China
[c] Department of Transfusion Medicine, School of Laboratory and Biotechnology, Southern Medical University, Guangzhou, China
[d] Key Laboratory of Advanced Mass Spectrometry and Molecular Analysis of Zhejiang Province, School of Material Science and Chemical Engineering, Ningbo University, Ningbo 315211, China
[e] Clinical Pharmacy Center, Nanfang Hospital, Southern Medical University, Guangzhou, China

ARTICLE INFO

Keywords:
Magnetic micro-living-motor
Bone metastasis
Precise medicine
Tumor model
Lung cancer

ABSTRACT

An ideal bone metastasis animal model is critical and fundamental for mechanistic research and following development of new drug and treatment. Caudal artery (CA) injection allows bone metastasis in the hindlimb, while in-depth targeted and quantitative studies of bone metastasis require a new model to overcome its limitations. Here, we developed a targeted, quantitative, and highly consistent method for the modeling of bone metastasis with cell-based magnetic micro-living-motor (MLM) system created by effectively combining Fe_3O_4-PDA-Au with biosafety. The MLM system can achieve efficient migration, target site colonization and control tumorigenesis in bone precisely with the application of a magnetic field. *In vivo*, day 3 post cell injection, tumor bone metastasis signals were observed locally in the injected femur among 82.76% mice of the MLM group as compared to the 56.82% in the CA group, and the signal intensity was 45.1 and 95.9 times stronger than that in the left and right lower limbs of the CA group, respectively. Post-injection day 28, metastasis *in vital* organs was reduced by approximately 90% in the MLM group compared to the CA group. Our innovative use of the MLM system in the field of tumor modeling opens a new avenue for exploring the mechanisms of tumor bone metastasis, recurrence and drug resistance.

1. Introduction

Bone metastasis is a common complication in advanced cancer patients, and bone is the third most common site of cancer metastasis. The occurrence of bone metastases always indicates poor prognosis. Non-small cell lung cancer is the third most susceptible tumor to bone metastasis, with 30–40% of patients developing bone metastasis during the course of the disease [1,2]. In addition to the damage to the body caused by tumor cells, tumor bone metastasis can also lead to a series of adverse events called skeletal-related events (SREs), including pain, pathologic fractures, spinal cord compression, malignant hypercalcemia and disability, resulting in a rapid decline in patient survival and quality of life [3].

Although remarkable achievements have been made in the early diagnosis and treatment of lung cancer, there is a lack of effective treatments for patients with bone metastasis. The main treatment for such patients is still primary tumor treatment and palliative therapy [4]. Tumor bone metastasis is a complex biological process involving multiple steps and factors [5]. The unclear mechanism is the most important factor restricting the development of effective treatments for tumor bone metastasis. Currently, there are several *in vivo* animal models available for studying bone metastasis. Intracardiac (IC) injection is the standard technique for studying the circulation extravasation and colonization of tumor cells. However, the technique is difficult to perform, and mice are prone to immediate mortality and metastasis of vital organs [6]. Tail vein injection (IV) is simple to perform, but tumor cells are more likely to remain in the lungs, while the incidence of bone metastasis is low [7–9]. *In situ* injection (*e.g.*, within the fat pad of the breast) may

* Corresponding author.
** Corresponding author at: Department of Haematology, Nanfang Hospital, Southern Medical University, Guangzhou, China.
E-mail addresses: ganning@nbu.edu.cn (N. Gan), jiangqianlid@qq.com, jiangql@smu.edu.cn (Q. Jiang).

https://doi.org/10.1016/j.colsurfb.2024.113877
Received 12 December 2023; Received in revised form 12 March 2024; Accepted 23 March 2024
Available online 27 March 2024

improve all stages of the cascade from primary tumor growth to distant metastasis, but metastasis after *in situ* injection is cell line-dependent and varies considerably in the frequency and location of secondary tumor growth [10,11]. *In situ* injection in the femur or tibia allows some tumor cells to remain localized in the bone, but a larger proportion of cells also enter the lungs [12,13]. Farhoodi et al. [14] used murine-derived breast cancer cells injected via the caudal artery (CA) to create a bone metastasis model that could be consistently detected after 2 weeks. Kuchimaru et al. [15] injected multiple human tumor cells (1×10^6) through the CA injection, and bone metastasis could be detected later. Tumor cells injected in the CA are forced to move upstream against the arterial blood flow for a short period before entering the femoral artery through the common iliac artery, eventually depositing and forming tumors in the hind limb bone but are not limited to bone tissue. Farhoodi et al. [14] showed that the metastasis rate of vital organs was 4.301% in the first week and 21.74% in the second week after caudal artery injection. The above modeling approaches demonstrate common limitations. First, the location of bone metastasis is not fixed, and there is a high risk of vital organ metastasis, which makes the stability and consistency between models poor, further affecting the reliability of subsequent experiments such as drug or immunotherapy. Second, human-derived cell lines or other cell lines with relatively slow metastatic development have low tumorigenic rates and long tumorigenic times using CA, which reduce the efficiency of follow-up studies and result in a short window for effective treatment.

The key to these problems lies in the low concentration of tumor cells at the target site, which might be overcome by developing a strategy to manipulate tumor cells to remain and grow precisely at the corresponding site by reducing the dissemination of tumor cell in other organs, which will limit immune clearance and promote robust colonization. Currently, micro/nanomotors and magnetic control strategies provide a solution to this challenge. Methods for manipulating the active delivery of micro/nanomotors show great potential in biomedicine. A variety of micromotor platforms have been developed thus far, including micromotors driven by external stimuli and biohybrid micromotors that combine cells, bacteria or algae with micro/nanocarriers [16–20]. They can be used for targeted drug/gene delivery, microsurgery, biopsy, tissue repair targeted tumor treatment, etc. [21–25]. Among them, cell-based biohybrid micromotors can be driven by magnetic [26–29], optical [30], acoustic [31,32], and electric fields [33] to move toward the target location based on a specified path, enabling targeted control.

Among various types of micromotors, magnetic fields and magnetic nanoparticles are commonly used in medical applications because of their clinical safety and tissue permeability [34]. Iron oxide nanoparticles such as maghemite (Fe_2O_3) and magnetite (Fe_3O_4) have been approved by the U.S. Food and Drug Administration (FDA) for diagnosis and treatment [35,36]. In addition, magnetically driven cells have garnered attention owing to their enhanced retention at the target site under magnetic field actuation. Wang et al. [37] showed that external magnetism increased the retention of super paramagnetic iron oxide nanoparticle (SPION)-labeled adipose-derived stem cells in the urethral sphincter and promoted the recovery of sphincter structure and function in a rat model of stress urinary incontinence. Similarly, Farshid Qiyami Hour et al. [38] demonstrated that the magnetic targeted cell delivery technique can effectively retain SPIONS-labeled human Wharton's jelly derived mesenchymal stem cells (MSCs) in the hippocampus of alzheimer's disease (AD) rats. Previous work by our team [13] has demonstrated that magnetically empowered luciferase-MSCs can move along the bone marrow cavity toward the magnet in the femur. Therefore, we developed a simple but effective strategy to achieve precise tumor formation in bone metastasis models using the magnetic micro-living-motor (MLM) system combined with an intra-bone marrow microinjector containing a syringe and a needle core invented by our team (patent no. 201620090904.2), mainly involving two steps (Fig. 1). First, the magnetic nanomotors magnetize the tumor cells to convert them into MLM, and then a precise magnetic field is used to navigate the MLM to promote targeted cellular colonization and proliferation in the

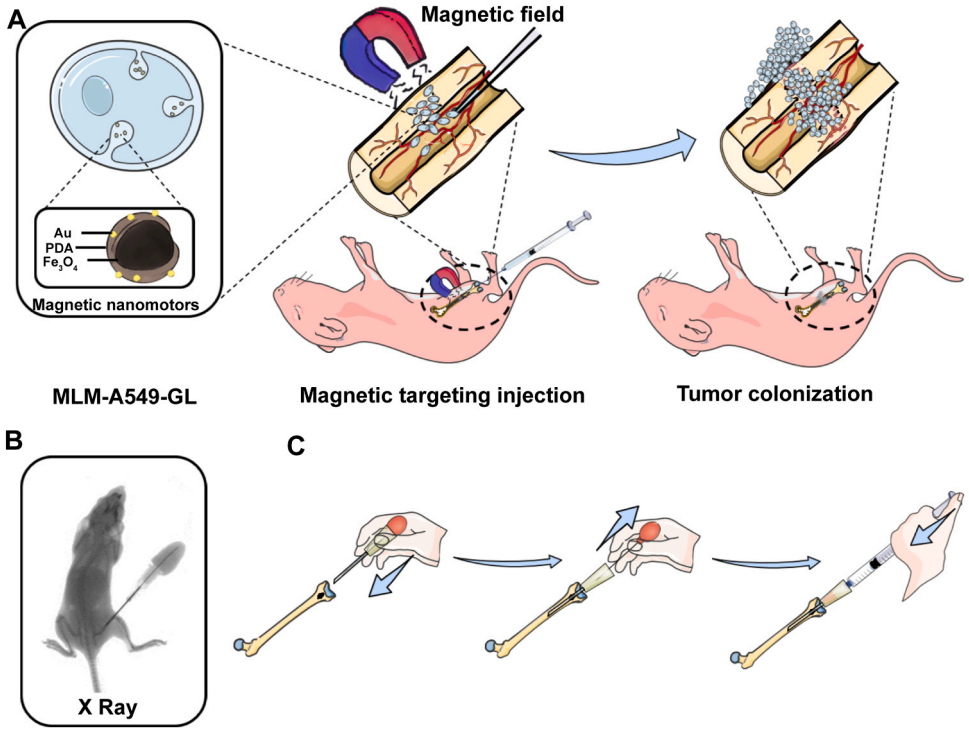

Fig. 1. Schematic diagram of the MLM system to construct a precision bone metastasis murine model. (A). Schematic diagram of magnetic nanomotors labeled A549-GL cells and MLM-A549-GL targeted femur colonization under the action of an applied magnetic field. (B). X-ray of successful intra-bone marrow injection. (C). The method of intra-bone marrow injection using a bone marrow microinjector containing a syringe and a needle core invented by our team (patent no. 201620090904.2).

bone marrow cavity, thus enabling precise modeling in bone.

The CA injection method is the latest method for constructing bone metastasis models that develop bone metastases predominantly in the hind limbs. In this study, we compared the tumor formation speed, bone metastasis rate, consistency and stability of the magnetic MLM system with CA by constructing a lung cancer bone metastasis model, as well as further evaluation its role in drug screening, mechanistic research, *etc*.

2. Materials and methods

2.1. Cell lines

The human alveolar adenocarcinoma cell line A549 was obtained from ATCC and modified with lentivirus carrying enhanced green fluorescence protein (eGFP) and the luciferase gene, namely, A549-GL cells. Cells were cultured in RPMI-1640 medium (Gibco, Invitrogen, Paisley, UK) containing 10% fetal bovine serum (FBS, Thermo Fisher Scientific) and 1% penicillin-streptomycin solution (Thermo Fisher Scientific) and incubated at 37°C and 5% CO_2.

2.2. Synthesis and characterization of magnetic nanomotors

The magnetic Fe_3O_4 core was synthesized via the coprecipitation reaction of iron(III) chloride and hydrated iron(II) chloride under alkaline conditions[39], followed by coating with a layer of dopamine (DA) and Au nanoparticles by self-polymerization to produce the Fe_3O_4-polydopamine-Au (Fe_3O_4-PDA-Au) composite [40]. In detail, 9.45 g $FeCl_3{\cdot}6\ H_2O$ and 6.94 g $FeCl_2{\cdot}4\ H_2O$ was dissolved in 160 mL of distill water and heated to 80 °C under nitrogen atmosphere. Next, add 20 mL of 25% ammonia slowly to the mixture while stirring at 400 revolutions per minute. Continue stirring for 10 h. The resulting precipitate was washed and separated using a magnet and distilled water until a pH of 7.0 was reached. Finally, the precipitate was washed with anhydrous ethanol four times and then vacuum dried at 70°C to obtain Fe_3O_4.

To prepare Fe_3O_4-PDA-Au, Specifically, 20 mg of tetrachloroauric acid, 10 mg of dopamine hydrochloride, and 200 mg of Fe_3O_4 were dispersed in 20 mL of 10 mM Tris-HCl buffer (pH 8.0, adjusted with 1 M HCl solution). The resulting mixture was then transferred to a 50 mL centrifuge tube and incubated on an overhead shaker (IKA® TRAYSTER, Staufen, Germany) at 50 rpm for 10 h at room temperature. Finally, the Fe_3O_4-PDA-Au was separated and washed in the same way as the Fe_3O_4.

The size, shape and distribution of Fe_3O_4-PDA-Au were detected by scanning electronic microscopy (SEM, S-3000 N, HITACHI, Japan), transmission electron microscopy (TEM, Tecnai G2 spirit BioTwin, FEI, USA) and energy dispersion X-ray spectroscopy (EDS). The hydrodynamic dimensions and zeta potential of the magnetic nanoparticles were determined using dynamic light scattering (DLS, Malvern Nano ZS, UK) with PBS as the dispersant.

2.3. Magnetizing A549-GL cells

A549-GL cells were cocultured with the magnetic nanomotors Fe_3O_4-PDA-Au, and the unbound Fe_3O_4-PDA-Au was washed away with phosphate-buffered saline (PBS). The cells were digested with 0.25% trypsin and then sorted with an Easy Sep Magnet (STEMCELL Technologies Singapore, Pte Ltd, Singapore) to obtain magnetized cells (hereafter designated MLM-A549-GL). A549-GL cells (10^6 cells/test, n=3) were incubated with different concentrations of Fe_3O_4-PDA-Au (20, 40, 80, 160 μg/mL) for different durations (3, 6, 9, 12, 24 h) to explore the optimal conditions for magnetized cells, and the selection rate was calculated based on the following formula: Selection rate = (Fe_3O_4-PDA-Au positive cell count after selection/total cell count before selection) ×100%. The interactions of cells with magnetic nanomotors were analyzed by both iron staining and TEM. For iron staining, MLM-A549-GL and A549-GL cell suspensions (2×10^5 cells/100 μL) were applied to slides, fixed with 4% paraformaldehyde and then stained with a Prussian blue staining kit (Solarbio Science & Technology Co., Ltd. Beijing, China) according to the manufacturer's instructions and observed under an orthomosaic microscope (BX63, OLYMPUS, Japan). For TEM, MLM-A549-GL cells were resuspended in 2.5% glutaraldehyde (Sigma-Aldrich Trading Co. Ltd, Shanghai, China) solution for 4 h and washed 3 times in PBS. The cells were fixed in 1% osmium tetroxide (SPI Supplies Division Structure Probe, Inc., USA) for 2 h and washed 3 times in PBS. The samples were dehydrated once (15 min) using a gradient of 50%, 70%, 80%, and 90% alcohol and twice (15 min) each in anhydrous ethanol and 100% acetone (Guangzhou Chemical Reagent, Guangzhou, China). Samples were soaked in a mixture of acetone and embedding solution, embedded in embedding agents and placed in embedding plates at 37°C for 24 h and 60°C for 48 h. The samples were cut into ultrathin sections of approximately 100 nm thickness using an ultrathin sectioning machine (EMUC7, Leica, Germany). Uranyl acetate and lead citrate (Shanghai Macklin Biochemical Technology Co., Ltd, Shanghai, China) were stained for 20 min and 12 min, respectively, and then observed by TEM (Tecnai G2 spirit BioTwin, FEI, USA).

2.4. Biological characteristics of MLM-A549-GL cells

Cell Counting Kit-8 (CCK-8, KeyGEN, Jiangsu, China) was used to detect whether magnetic nanomotor labeling affects cell viability. A549-GL cells were seeded in 96-well plates (10^4/well, n=3) with 200 μL of complete medium per well. After 6 h of culture, magnetic nanomotors were added at concentrations of 20, 40, 80, and 160 μg/mL, and no magnetic nanomotors were added as the control group. After 3 h, 6 h, 12 h, 24 h or 2–7 d of culture, 10 μL of CCK-8 reagent was added to each well and incubated for 2 h at 37°C. Cell viability was analyzed by optical density at 450 nm using an enzyme-labeled instrument (MB580, Huisong, China) using the following formula: Cell viability (%) = OD (experimental) /OD (control) × 100%.

Flow cytometry was used to detect whether magnetic nanomotor labeling affects the apoptosis of cells. Magnetic nanomotors were cocultured with A549-GL cells at different concentrations (20, 40, 80, and 160 μg/mL) for 12 h, and those without magnetic nanomotors were used as the control group (1×10^6 cells/test, n=3). Apoptosis was detected by flow cytometry (FACS Calibur, Becton Dickinson Inc., New Jersey, USA) according to the product instructions (Annexin V-Alexa Fluor 647/PI Apoptosis Detection Kit, Cat. 40304ES50, Yeasen, China).

2.5. Migration characteristics of MLM-A549-GL cells under a magnetic field in vitro

The targeted migration of MLM-A549-GL cells under an external magnetic field was observed *in vitro*. The MLM-A549-GL or A549-GL cell suspension (3×10^6/20 μL) was injected into a counting plate (Python-Bio, Guangzhou, China). The specifications of each well of the counting plate were 0.9×0.7×0.19 mm, sealed on three sides, and one side with cells. A small square magnetic field (5×1.5×1 mm, 260 mT) was applied or not outside the plate and did not contact the cell suspension. The movement of the cells was observed and recorded by a microscope (Axio Zoom. V16, ZEISS, Germany).

2.6. Targeted colonization of MLM-A549-GL cells under a magnetic field in vitro

Tumor formation was simulated *in vitro* under the effect of an applied magnetic field. MLM-A549-GL or A549-GL cells (2×10^4 cells/2 mL) were inoculated in 24-well plates with a square magnetic field (5×1.5×1 mm, 260 mT) fixed at the bottom of each plate, and the magnetic field was withdrawn after 12 h of incubation (37°C, 5% CO_2). The growth distribution of the cells was observed under an inverted fluorescence microscope (IX73, OLYMPUS, Japan) and the colonization rate was calculated according to the following formula: Colonization

rate = [(A549-GL cell count) – (non-aggregated MLM-A549-GL cell count)] / A549-GL cell count ×100%.

2.7. Construction of bone metastasis models

BALB/c-nu mice (female, 4–6 w) were obtained from SIPEIFU (Beijing) Biotechnology Co., Ltd. All mice used were maintained in a specific pathogen-free (SPF) barrier system at the Laboratory Animal Centre of Nanfang Hospital, Southern Medical University [Facility Use Certificate No: SYXK (GD) 2023–0056]. All experimental procedures were approved by the Laboratory Animal Use Management Committee. For the *in vivo* experiment, 90 BALB/c-nu mice were randomly divided into the MLM group (injection into the femoral bone marrow via an intrabone marrow microinjection syringe designed by our team with local magnetism, Fig. 1B, C, n=30) and the CA group (injection into the caudal artery without local magnetism, n=60).

For CA injection, MLM-A549-GL cells (1× 10^6 cells) suspended in 200 μL PBS were injected into the CA of mice for a short time with an insulin needle (29 G, 0.33×12.7 mm, Becton Dickinson Inc., New Jersey, USA) [15], and sterile cotton balls were pressed at the location of the entry point of the needle.

For MLM injection, all mice were anesthetized with sodium pentobarbital (0.2–0.3 mL 0.3% w/v in PBS per mouse), the puncture site was adequately sterilized, and the procedure was performed under aseptic conditions. Femoral puncture was performed under X-ray guidance (Ami HTX, Spectral Instruments Imaging, USA, X-ray source=10–40 keV, X-ray field of view=25×15 cm) using a bone marrow microinjector containing a syringe and a needle core invented by the authors' team , and a precise magnetic field (5×1.5×1 mm, 260 mT) was applied to the femoral fixation site. The needle core was withdrawn, and MLM-A549-GL cells (1×10^6 cells) suspended in 20 μL PBS were slowly injected into the bone marrow cavity. Sterile cotton swabs were pressed to stop bleeding after removal of the injection needle, and the magnetic field was removed after 24 h.

2.8. In vivo bioluminescence imaging

Mice were injected intraperitoneally with 100 μL D-luciferin potassium salt (10 mg/mL, PerkinElmer, USA) and imaged for bioluminescence (BL) signals using a small animal live imaging system (Ami HTX, Spectral Instruments Imaging, USA) at 5–10 minutes postinjection (exposure time=60 s, field of view=25×17 cm, f/STOP=1.2). Overlaying bright-field images and BL images was used to analyze the location of tumor signals. The BL images were analyzed by Aura software specialized for Ami HTX.

2.9. Bioluminescence imaging of isolated bone and organs

Mice were injected intraperitoneally with 100 μL of D-luciferin potassium salt (10 mg/mL, PerkinElmer, USA), and the organs and hind limb were rapidly separated within 5–10 min. Signal acquisition was performed using a small animal *in vivo* imaging system (Ami HTX, Spectral Instruments Imaging, USA), and analysis of tumor signal location was performed by overlaying bright-field images and BL images.

2.10. Micro-MRI

Mice were anesthetized with isoflurane (oxygen delivered at 0.5 L/min with 3% isoflurane for induction and 1.5% isoflurane for maintenance), MRI imaging was performed on a 7 Tesla ultrahigh field MRI scanner (Pharma Scan 70/16, US, echo time (TE)=35 ms, repetition time (TR)=2500 ms, slice thickness (SL)=0.7 mm, image size=256×256 mm, field of view (FOV)=20×20 mm), and data were analyzed with RadiAnt DICOM Viewer 2022.1.1.

2.11. Micro-PET/CT imaging

Tumor growth was observed in mice using positron emission tomography (PET; IRIS PET/CT, Inviscan, Strasbourg, France) 14 d after cell injection (+14 d). Mice were fasted for 12 h and injected with 3.62 ± 0.55 MBq (125 μL) $^{[18\,F]}$ FDG via the IV. To prevent tracer uptake by the leg muscles, anesthesia was maintained via intraperitoneal sodium pentobarbital (0.2–0.3 mL 0.3% w/v in PBS solution per mouse), and body temperature was maintained with a 37°C heating pad. After 40 min, the mice were placed in the central field of the scanner for a 10 min static emission PET scan. The mice were kept under anesthesia with isoflurane during the shooting period. PET/CT images were visualized and analyzed using RadiAnt DICOM Viewer 2022.1.1.

2.12. Micro-CT imaging

For micro-CT imaging, the mice were sacrificed by cervical dislocation at +28 d, and the femur was isolated. The signal acquisition of bone tissue was performed by micro-CT (Micro CT81 SCANCO MEDICAL AG, Switzerland) and analyzed by MIMICS.

2.13. Histological analysis

The tumor-bearing femur was taken for histological analysis after the mice were sacrificed. The isolated femurs were fixed in 4% paraformaldehyde (DF0135, LEAGENE, China) for 24 h and then decalcified in EDTA decalcifying solution (G1105, Servicebio, China) for 4 weeks. After paraffin embedding, they were stained with a hematoxylin-eosin staining kit (G1120–10, Solarbio, China) after being cut into 5-μm-thick coronal longitudinal sections. HE-stained images were taken with an orthomosaic microscope (BX63, OLYMPUS, Japan).

2.14. Statistical analysis

Statistical analysis was performed using SPSS Statistics 25.0 software version. For two-group comparisons, continuous data obeying a normal distribution with equal variance were used in the two-side student's t-test; if the above conditions were not met the Independent-Samples Mann-Whitney U Test was used. For multiple group comparisons, One-Way ANOVA and Tukey's test multiple comparisons were used for continuous data obeying a normal distribution with equal variance, otherwise, Kruskal-Wallis H and multiple comparisons were used. Pearson Chi-Square was used for categorical data. All data are expressed as the mean ± SD or quartiles. The threshold for significance for all experiments was set at $^*p < 0.05$, and smaller p values are represented as $^{**}p < 0.01$ and $^{***}p < 0.001$.

3. Results and discussion

3.1. Synthesis and characterization of magnetic nanomotors

Fe_3O_4-PDA-Au magnetic nanomotors were successfully prepared by coprecipitation methods. The morphology and element analysis of Fe_3O_4-PDA-Au were characterized using SEM and EDS. The Fe_3O_4-PDA-Au exhibits a uniform spherical morphology and aggregate in the magnetic field of the SEM due to their superparamagnetism (Supplementary Figure 1 A). However, in the absence of a magnetic field, they can be well dispersed in the culture medium. EDS mapping and spectrum display the distribution of Fe, Au, C, N and O elements in Fe_3O_4-PDA-Au (Supplementary Figure 1). The TEM results showed that the nanostructure was composed of an Fe_3O_4 magnetic core and a composite shell consisting of PDA and Au nanoparticles (Fig. 2A). The peak hydrodynamic diameter distribution measured by DLS was 142.4 nm (Fig. 2B), with an average particle size of 202.7 nm, which is close to the diameter observed by SEM (206.54 ± 58.81 nm). The particle size distribution was narrow, and the polydispersity index was 0.346. Zeta potential

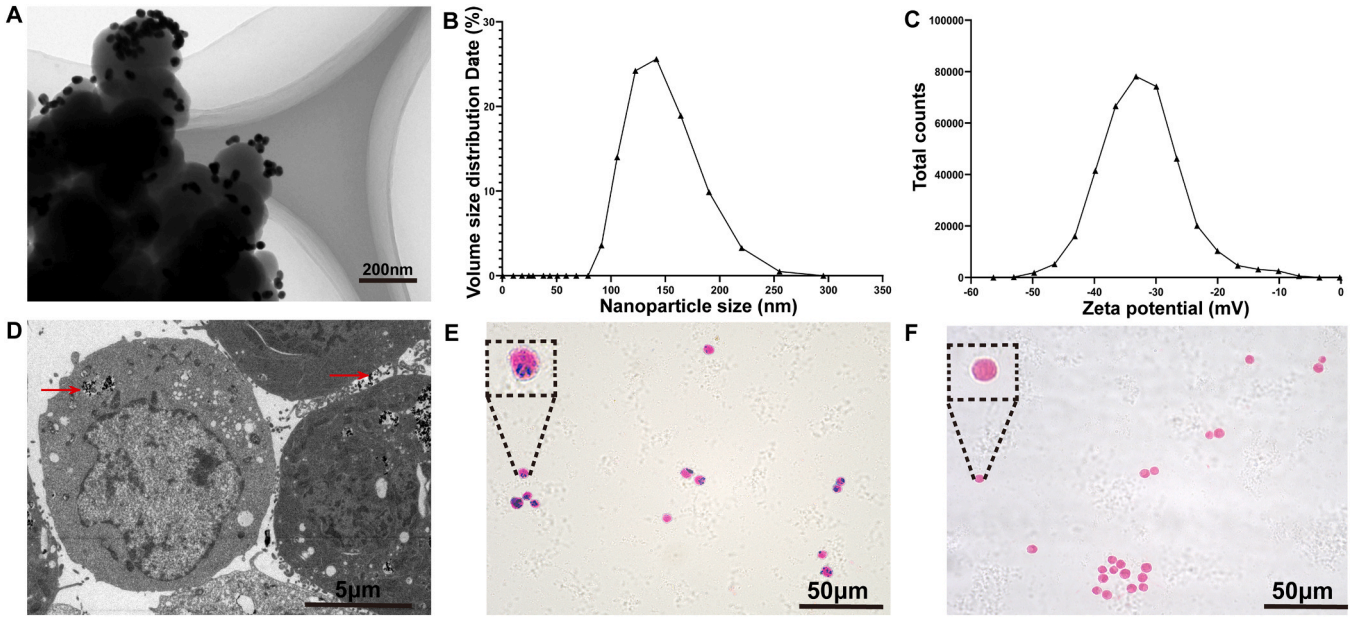

Fig. 2. Characterization of magnetic nanomotors. (A). TEM images of Magnetic nanomotors. (B). DLS analysis magnetic nanomotors size distribution. (C). Z-potential by DLS analysis. (D). Representative TEM images of MLM-A549-GL cells, the red arrows indicate magnetic nanomotors attached to the cell surface or internalized into the cell. (E). Iron staining of MLM-A549-GL cells. (F). Iron staining of A549-GL cells.

analysis showed that Fe_3O_4-PDA-Au had a high density of negative charges with an absolute value of −32.8 mV (Fig. 2C), which could improve its dispersion stability in solution through strong electrostatic interactions.

3.2. Preparation of MLM-A549-GL cells

A549-GL cells were magnetized with magnetic nanomotors, and TEM images showed that magnetic nanomotors were internalized into the cytoplasm or adsorbed on the surface of the cell membrane, magnetic nanomotor phagosomes were visible, and the cell membrane and organelles were structurally intact (Fig. 2D). Iron staining showed that magnetic nanomotors were distributed in the cytoplasm of MLM-A549-GL cells (Fig. 2E, F). To explore the optimal magnetization conditions of A549-GL cells, we analyzed the effects of different concentrations of magnetic nanomotors (0, 20, 40, 80, and 160 μg/mL) and different magnetization times (3, 6, 9, 12, and 24 h) on the magnetization efficiency of cells. MLM-A549-GL cells were obtained by magnetic sorting. Trypan blue staining showed that the proportion of rejected living cells was 99.49% ± 0.18 (n=3). According to the formula, the magnetization selection rate increased with increasing magnetization time (Fig. 3A, $P<0.001$), and there was no significant difference at 12 h and 24 h. (Fig. 3A, $P>0.05$). We chose 12 h as the time for magnetization of A549-GL cells. The magnetization selection rate of A549-GL cells also increased with increasing concentrations of magnetic nanomotors (Fig. 3B). However, it showed cytotoxicity when the concentration reached 160 μg/mL (Fig. 3C, $P<0.05$), so A549-GL cells were cocultured with magnetic nanomotors at a concentration of 80 μg/mL for 12 h to magnetize the cells.

3.3. Biological characteristics of MLM-A549-GL cells

Cell viability was assessed using the Cell Counting Kit-8 (CCK-8) after coculturing A549-GL cells (2×10^4 cells/test, n=3) with magnetic nanomotors at different concentrations (0, 20, 40, 80, 160 μg/mL) for 3, 6, 12, and 24 h. The cell viability did not show statistically significant differences across different time points and concentrations of magnetic nanomotors ranging from 0 to 80 μg/mL (Fig. 3C, $P>0.05$). Further, A549-GL cells (1×10^4 cells/test, n=3) were co-cultured with 80 μg/mL magnetic nanomotors for 2–7d. The effect of magnetic nanomotors on long term cell viability was evaluated using CCK-8, and the difference was not statistically significant (Supplementary Figure 2, $P>0.05$). Moreover, apoptosis was examined using an Alexa Fluor 647/PI apoptosis detection kit after coculturing A549-GL cells with magnetic nanomotors at different concentrations (0, 20, 40, 80, 160 μg/mL, 1×10^6 cells/test, n=3) for 12 h. The results showed that the cell survival rates were 95.9% ± 0.53, 95.13% ± 0.90, 97.00% ± 1.56, 97.33% ± 0.38, and 97.00% ± 0.17, respectively. The difference was not statistically significant (Fig. 3D, E $P>0.05$). The above results showed that Fe_3O_4-PDA-Au magnetic nanomotors have good biocompatibility.

3.4. Targeted manipulation of MLM-A549-GL cells under a magnetic field in vitro

We monitored the targeted migration characteristics of MLM-A549-GL cells in a finite fluid in a counting plate (Fig. 3F). Time-lapse photography under a stereomicroscope showed that A549-GL cells are unaffected by the magnetic field in liquid and undergo slow Brownian motion (Supplementary Movie 1), and MLM-A549-GL cells can only move slowly in Brownian motion in the absence of a magnetic field but can undergo accelerated motion toward the position of the strongest magnetic force under the influence of a magnetic field, with an average velocity of 1817.91 ± 643.70 μm/s (Fig. 3G and Supplementary Movie 2).

Supplementary material related to this article can be found online at doi:10.1016/j.colsurfb.2024.113877.

3.5. Targeted colonization of MLM-A549-GL cells under a magnetic field in vitro

We simulated tumor formation under an external magnetic field *in vitro* to observe MLM-A549-GL cell characteristics of targeted colonization at specific locations. After 12 h of exposure to the external magnetic field, MLM-A549-GL cells achieved site-directed growth under a fluorescence inverted microscope with a distribution pattern consistent with the magnetic field, and their colonization rate was 79.54 ±1.38%, whereas A549-GL cells grew uniformly and diffusely (Fig. 3H) on the bottom of the well plate.

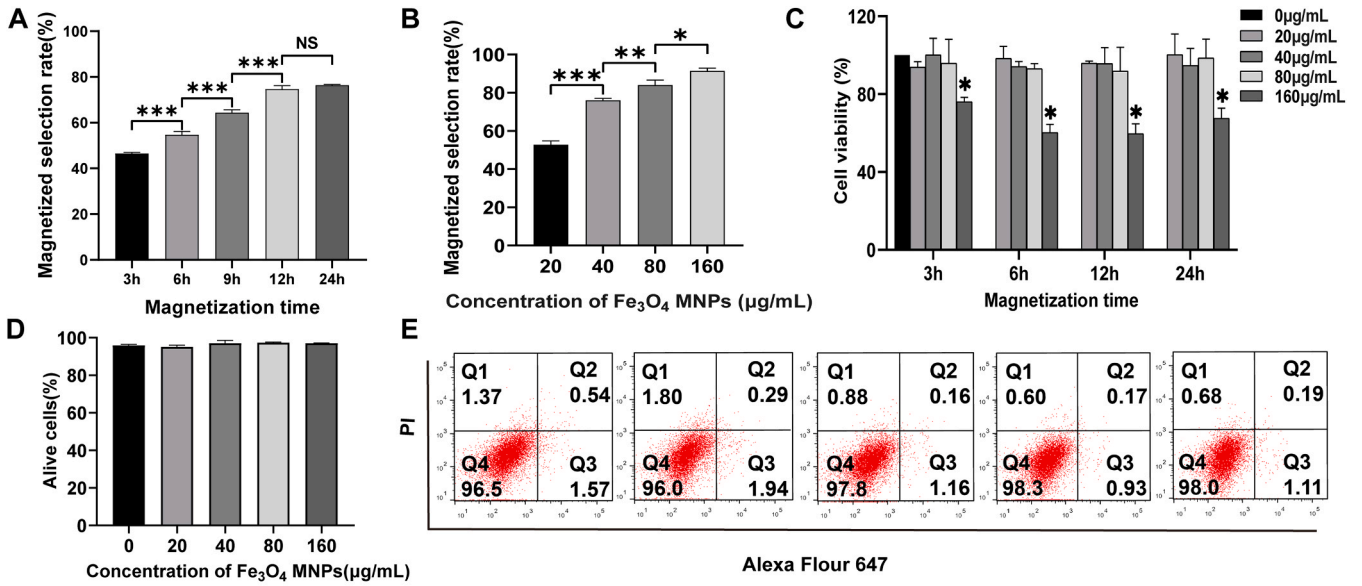

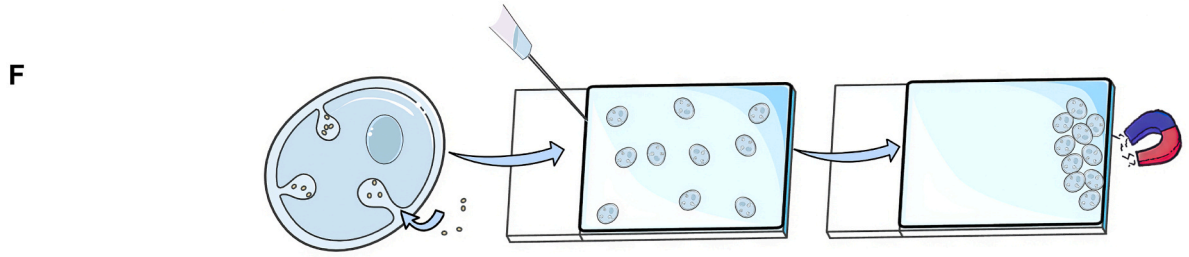

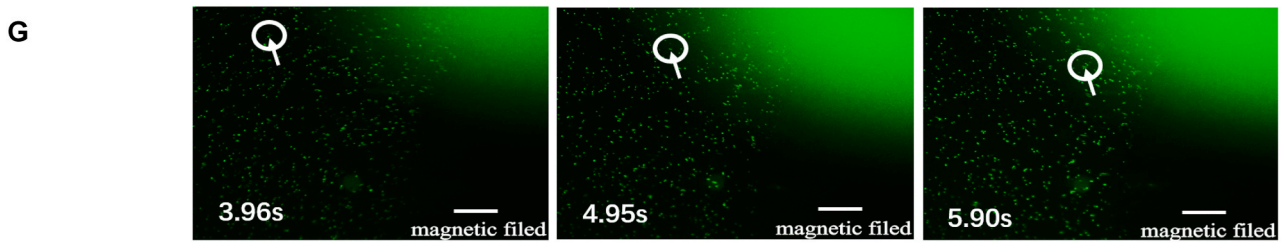

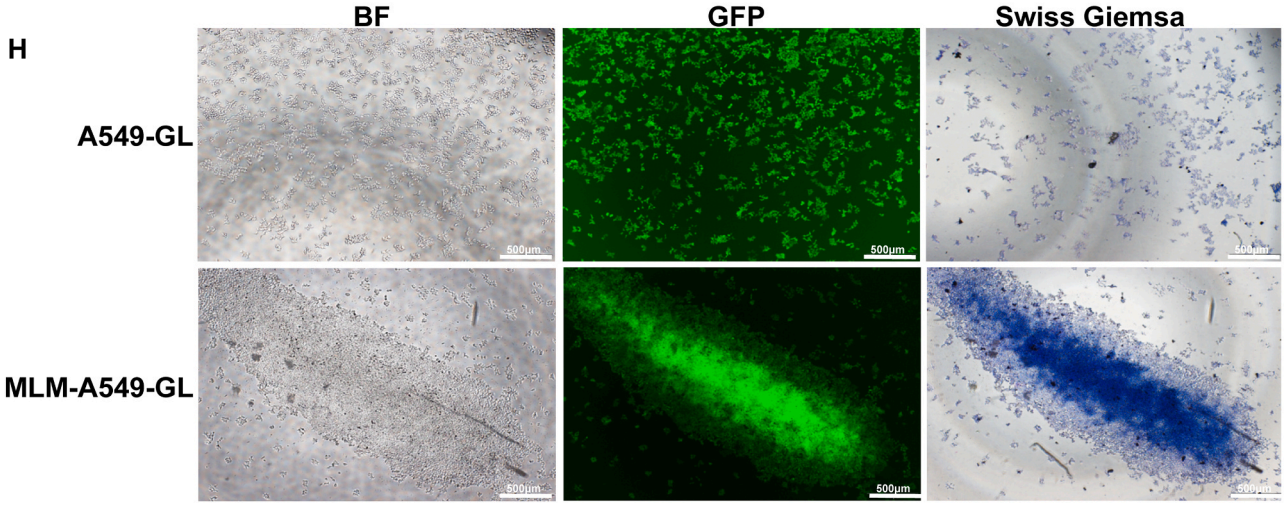

(caption on next page)

Fig. 3. Viability, apoptosis, magnetization conditions, migration and colonization of MLM-A549-GL cells. (A). Magnetic nanomotors magnetization efficiency of A549-GL cells is correlated with magnetization time. 1×10^6/test, n=3, (One-Way ANOVA and Tukey's test multiple comparisons), Error bars indicate SD. ***P < 0.001, NS means no statistical difference. (B). Magnetic nanomotors magnetization efficiency in A549-GL cells in various concentration. 1×10^6/test, n=3, (One-Way ANOVA and Tukey's test multiple comparisons). Error bars indicate SD. *P < 0.05, **P < 0.01, ***P < 0.001. (C). Cell viability of A549-GL cells co-cultured with magnetic nanomotors at different concentrations and times. 2×10^4cells/test, n=3, (two side student's t-test), Error bars indicate SD. *P<0.05. (D). Quantitative data on living cells in apoptosis analysis (%). (E). Flow cytometric analysis of apoptosis in MLM-A549-GL cells magnetized with different concentrations of magnetic nanomotors for 12 h. 1×10^6/test, n=3, (two side student's t-test). Error bars indicate SD. (F). Schematic diagram of *in vitro* migration experiment. MLM-A549-GL cells were filled in the cell counting plate under the posture microscope, and the magnetic field was applied locally. (G). MLM-A549-GL cells moves rapidly in the direction of the magnetic field. White arrows indicate the MLM-GL-A549 cells (Scale bar: 2000μm). (H). Distribution of A549-GL cells and MLM-A549-GL cells under magnetic field. The colonization shape of MLM-A549-GL cells is consistent with the shape of the magnetic field.

3.6. Precision magnetism induced MLM-A549-GL cells to colonize the femur

Our prevalidation experiments [13] showed that the BL signals of the intra-femoral bone marrow injection (IB) and IV methods were mostly located in the lungs 30 min after cell injection and could not specifically colonize the bone (Supplementary Figure 3). Therefore, in this study, we focused on using the magnetic MLM system to improve intramedullary infusion to promote cell colonization in bone. For the in vivo experiment, 29 (96.67%) in the MLM group and 44 (73.33%) in the CA group were successfully injected, with significant differences (P=0.008). The high success rate of MLM group injection is due to the simplicity and stability of the method. With the help of our team's patented tools, it took only a few minutes to create a model. The traditional bone marrow injection method for creating a model has a higher failure rate due to the blocking of the needle by bone tissue during bone penetration and requires a second injection. In addition, direct injection of cells through an insulin needle may cause extravasation of cells outside the targeted area and result in inconsistency in the doses of cells injected in different mice [12,41]. Here, we used a self-designed bone marrow microinjector containing a syringe and a needle core, which can avoid problems such as needle clogging and cell extravasation. With the assistance of an external magnetic field, the method can deliver tumor cells directly and precisely to their preferred implantation site with minimal cell loss, allowing for the establishment of a tumor model and effectively increasing the success, precision and repeatability of intraosseous cell injection.

At 30 min after cell injection, BL signals were detected. In the MLM group, the signals were specifically concentrated in the femur of the injection side, while the signals in the CA group were mainly distributed in the lower body and part of the lungs of the mice (Fig. 4A). Furthermore, in the MLM group, the femur BL signal intensity was relatively uniform among different individuals, and there was a very small amount of signal in the lungs, which was significantly lower than that in the CA group (Fig. 4B, P<0.05). We also tried CA injection combined with a femoral localized magnetic field (CAM), but unfortunately, there were still more BL signals in the lungs (Supplementary Figure 4). Previous work by our team [13] has demonstrated that in the MLM group, if the local magnetic field is removed from the femur within 1 h, the magnetized cells will re-enter the circulation and be mainly distributed in the lungs in approximately 5 min. These results demonstrated that the magnetic MLM system specifically enhances cell accumulation in the femoral bone marrow cavity.

In the CA group, BL signal aggregation was observed in the bilateral or unilateral knee joint of the mice at +3 d but quite weak and unstable. BL intensity gradually increased from +3 d to +28 d, there was no significant difference between bilateral femurs (P>0.05), and the BL intensity was inconsistent among individuals with bone metastases. However, in the MLM group, isolated, consistent, and gradually increasing BL signals were observed in the injected femur from +3 d to +28 d (Fig. 4A), with +3 d intensities that were 45 and 95 times higher than those in the left and right lower limbs of the CA group, respectively (Fig. 4C, P<0.001). No clear BL signal was observed in the contralateral femur. The comparison of bilateral femur BL strength between the two groups at different times is shown in Supplementary Table 1.

3.7. General conditions and bone metastasis rate

We performed a control analysis between the MLM group and the CA group and compared the development of bone metastasis in mice in the two groups by observing the changes in BL intensity over time (30 min, +3, +7, +14, +21, +28 d) after injection of MLM-A549-GL cells (Fig. 4A). BL imaging showed that the bone metastasis rates of the MLM group (n=29) and CA group (n=44) were 82.76% and 56.82% at +3 d (P=0.021), 82.76% and 45.50% at +7 d (P=0.001), and 82.76% and 50.00% at +14 d (P=0.005), respectively. The bone metastasis rate of the CA group decreased first and then increased within 14 d, while the bone metastasis rate of the MLM group remained stable, and all were *in situ* (Fig. 4D). Thus, the magnetic MLM system could significantly improve the bone metastasis rate of lung cancer cells, which may improve the success rate of constructing models using cell lines that are less likely to form tumors or with patient-derived cells.

At the same time, the general conditions of the two groups were compared. Ten mice were randomly selected, and their body weight (Fig. 4E) was measured weekly starting from the day of injection. The mice in the MLM group (n=10) were in a normal behavioral state, and there was no significant difference in body weight between the two groups in the first two weeks (P>0.05). After +21 d, the body weight of mice in both groups decreased, while the average body weight of mice in the MLM group was significantly higher than that in the CA group at +21 d (P=0.025) and +28 d (P=0.009).

3.8. In vivo tissue distribution of MLM-A549-GL cells

BL imaging of the isolated hind limb showed that the femur on the injection side of the MLM group exhibited a strong BL intensity at +14 d, and no clear signal was detected in the contralateral femur; on day +28, the femur BL intensity increased, and the contralateral femur was visible within a specific BL color range (Supplementary Figure 5). While in the CA group, BL signals were visible in both femurs at +14 d and +28 d (Fig. 5A). *In vitro* organ BL imaging showed that at +14 d, weak signals could only be detected in the lungs of the MLM group, whereas clear signals were observed in the liver and lungs of the CA group (Fig. 5B); on day +28, the MLM group showed a 99.85%, 98.67%, 89.51% and 98.79% reduction in liver, lungs, kidney and spleen, respectively, compared with the CA group. Weak signals were observed only in the brain, liver and lungs in the MLM group, while cancer cells spread to all tissues in the CA group (Fig. 5B), including the brain (P=0.248), liver (P<0.05), lungs (P<0.05), both kidneys (P<0.05) and spleen (P<0.05, Fig. 5C), and an infiltrated ovarian tumor was observed in a mouse of CA group, with tumors up to 1.1 cm×1 cm (Supplementary Figure 6).

Early tumor formation was detected by micro-MRI and micro-PET/CT at +14 d, and tumor cell distribution was assessed by micro-MRI, micro-CT and histology at +28 d. Micro-MRI results of +14 d (Fig. 6A) showed that in the MLM group, there was visible tumor tissue outside the bone, with clear low signals near the metaphysis endpoint, likely due to the presence of Fe_3O_4 nanoparticles that show low signal intensity on T2 images [21]. No clear tumor tissue was found in the contralateral femurs. In the CA group, tumor growth was observed in the femur bilaterally with a high signal, but no clear tumor tissue was observed outside the bone. $^{[18\,F]}$ FDG imaging performed at +14

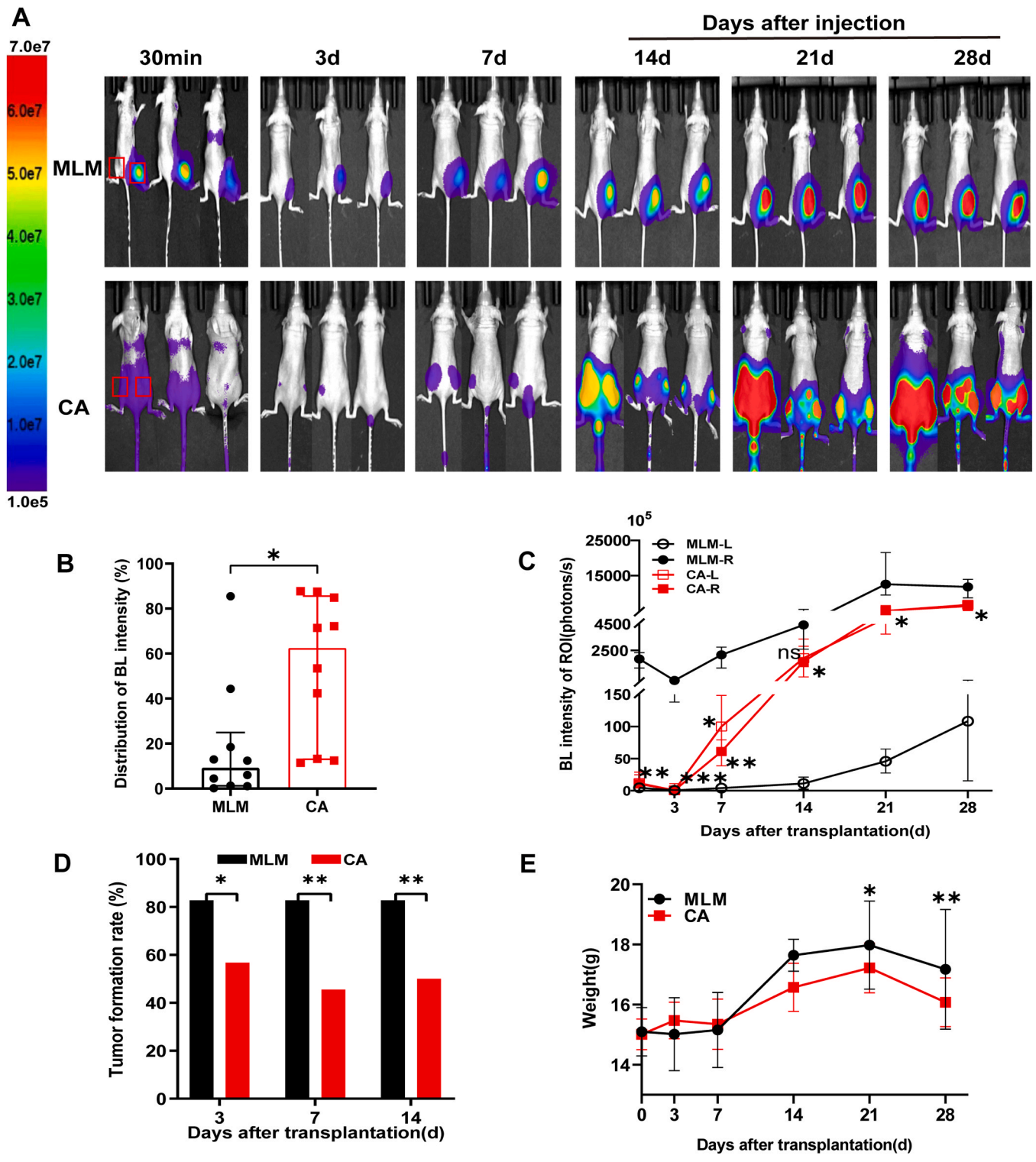

Fig. 4. The MLM system improves tumor femur bone metastasis rate. (A). Representative BL images at indicated days after MLM (n=10) and CA (n=10) injection of MLM-GL-A549 cells. (B). Ratio of lung BL intensity to whole-body BL intensity 30 min after MLM (n=10) and CA (n=10) injection of MLM-GL-A549 cells, (Independent-Samples Mann-Whitney U Test). Error bars indicate quartiles. *P < 0.05. (C). BL intensity in region of interest (ROI) at indicated days after MLM (n=10) and CA (n=10) injection of MLM-GL-A549 cells. Red boxes in the images of 30 min indicate ROI, and bilateral femur of CA group compared with MLM-R statistics are labeled in the figure. (Kruskal-Wallis H and multiple comparisons). Error bars indicate quartiles. *P< 0.05, **P < 0.01, ***P < 0.001, ns means no statistical difference. (D). Bone metastasis rates at 3 d, 7 d and 14 d after MLM-A549-GL cells injection by MLM (n=29) and CA (n=44). *P < 0.05, **P < 0.01 (Pearson Chi-Square). (E). Body weight changes on specified days after MLM-A549-GL cells injection by MLM (n=10) and CA (n=10). (two side student's t-test). Error bars indicate SD. *P< 0.05, **P < 0.01.

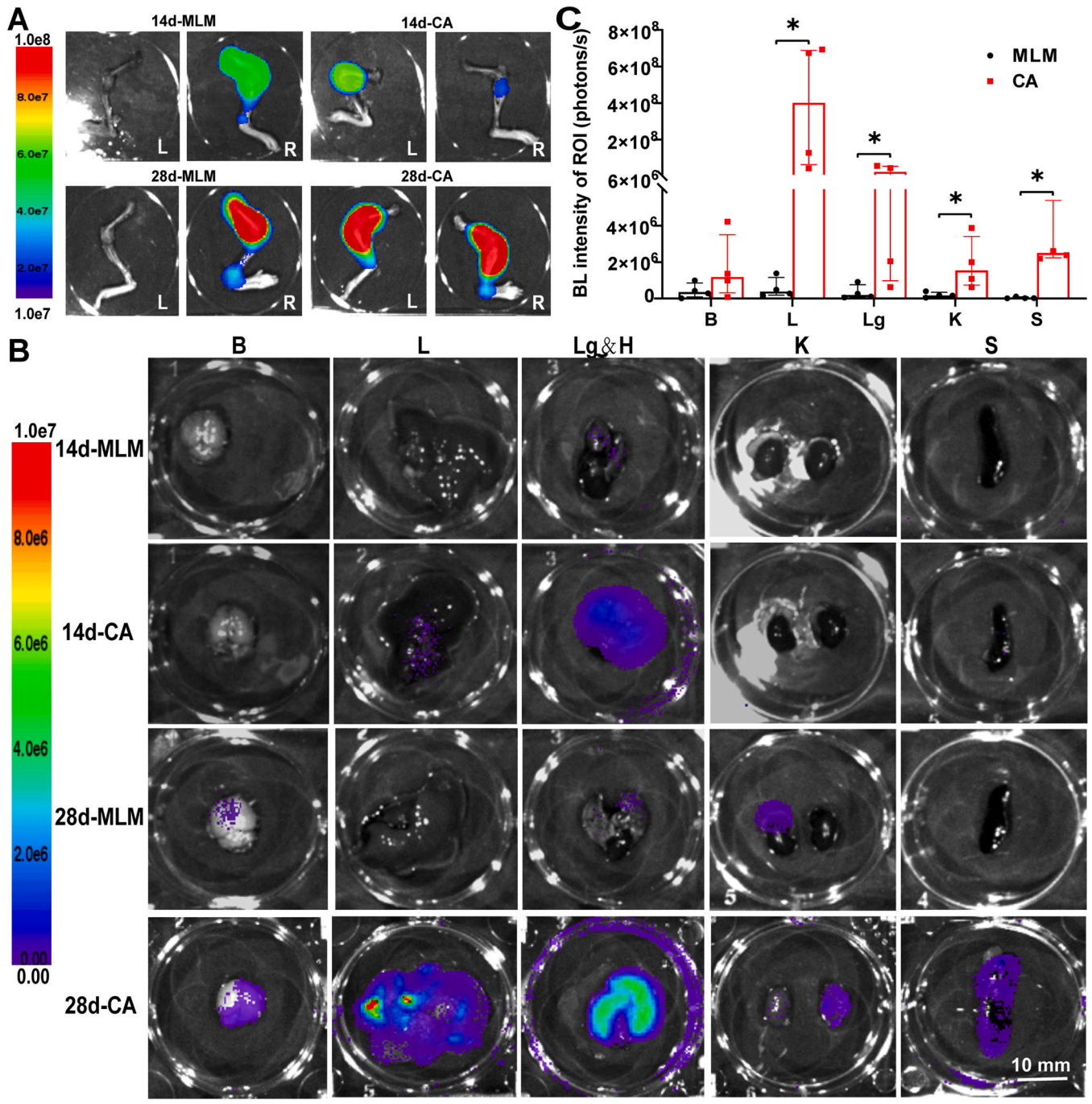

Fig. 5. The MLM system enables precise femur tumor formation. (A). Representative BL images of both lower limbs at 14 d and 28 d after MLM-A549-GL cells injection by MLM and CA. (B). Representative *in vitro* BL images of organs harvested from mice at 14 d and 28 d after MLM-A549-GL cells injection by MLM and CA. B brain, Lg lung, H heart, S spleen, Lv liver, K kidney. (C). BL intensity of each organ at 28 d after MLM-A549-GL cells injection by MLM (n=4) and CA (n=4), (Independent-Samples Mann-Whitney U Test). Error bars indicate quartiles. *P < 0.05.

d (Fig. 6C) showed that uptake of $^{[18\ F]}$ FDG in the femur on the injection side of the MLM group was stronger than that in the bilateral femur of the CA group. Micro-MRI results showed that the tumor tissue in both groups increased in size at +28 d. In the MLM group, a weak high signal was seen in the contralateral femur, and no clear tumor tissue was seen outside the bone. In the CA group, tumor tissue was seen outside the femur, tibia and knee joint bilaterally, which was consistent with the BL results. *In vitro* femoral micro-CT results (Fig. 6B) confirmed that there was significant bone destruction on the injected side of the femur in the MLM group at +28 d.

To adapt to the bone marrow microenvironment, circulating tumor cells are temporarily dormant in the bone marrow [42]. Lawso et al. [43, 44] found that dormant myeloma cells directly adjacent to the endosteal bone surface were occupied by osteoblasts expressing type I collagen, while proliferating myeloma cells tended to occupy positions away from the bone surface. Interestingly, HE staining of pathological sections of femur results (Supplementary Figure 7) showed that the tumor grew in aggregates close to the bone surface on the injection side of the MLM group at +14 d, which may be due to the initial local colonization of MLM-A549-GL cells under the effect of the magnetic field. This will provide a research model to explore the key mechanisms of dormancy in osteoclasts, osteoblasts and tumor cells in virous tumors, as well as the

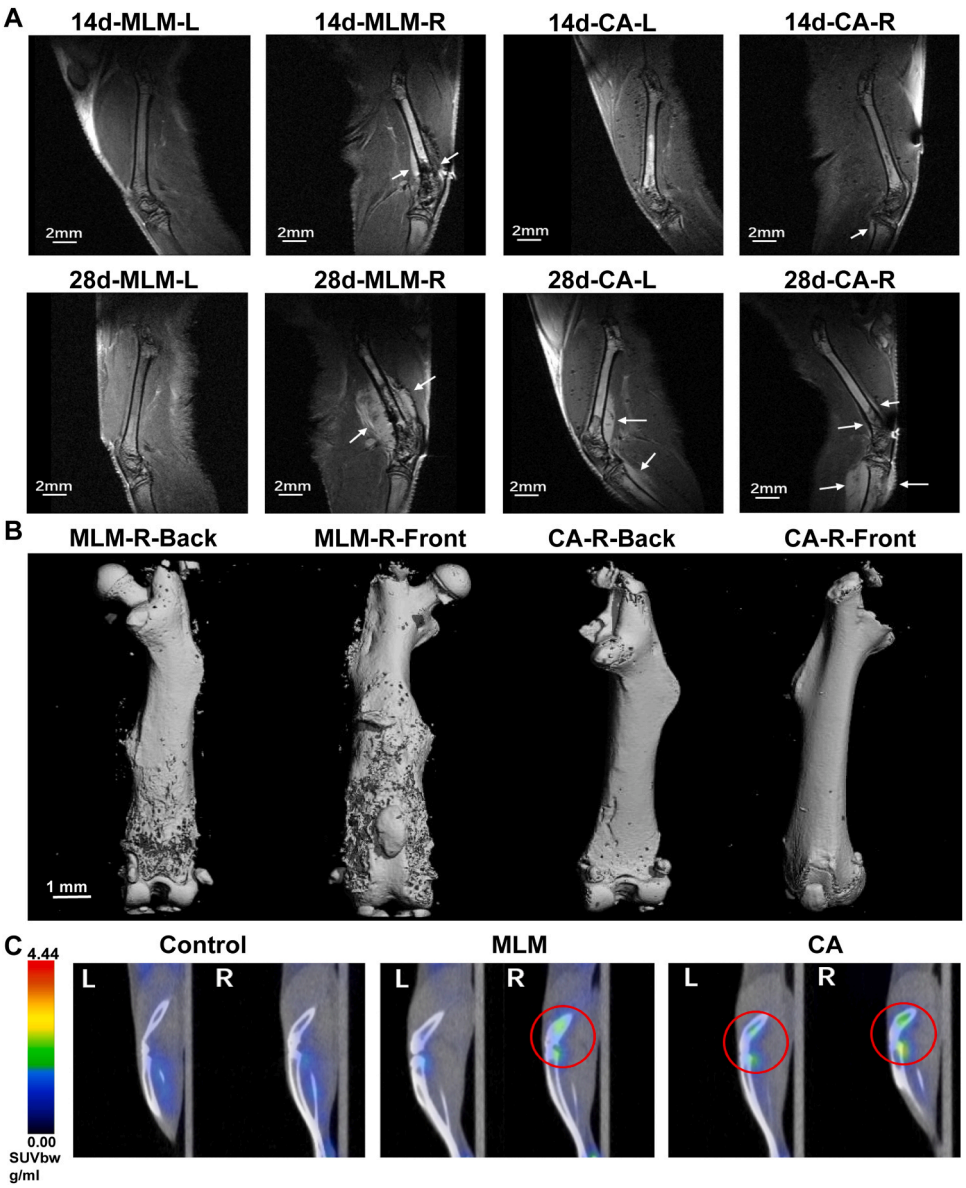

Fig. 6. Detection of hindlimb bone metastases in mice using MRI, Micro-CT and $^{[18\,F]}$ FDG PET/CT. (A). Representative coronal T2-weighted MR images of the mouse femur at 14 d and 28 d after MLM-A549-GL cells injection by MLM and CA. White arrows indicate the location of bone metastases. (B). Representative micro-CT 3D reconstructions of the femur in normal mice and at 28 d after MLM-A549-GL cells injection by MLM. (C). Representative hindlimb $^{[18\,F]}$ FDG PET/CT images of normal mice and 14 d after MLM-A549-GL cells injection by MLM and CA. Red circles indicate the location of bone metastases.

interaction between cells and molecules in the bone marrow microenvironment and to develop of therapeutic approaches to prevent tumor bone metastasis. On day +28, tumors in the isolated femurs of the MLM group grew diffusely in the bone marrow cavity of the lower 2/3 segment of the femoral body on the injection side (Supplementary Figure 8). HE staining results also confirmed this, and a demarcation between normal bone tissue and tumor tissue was observed. Tumor cells were also observed in the contralateral femur, suggesting that the tumor progressed to the contralateral femur at a later stage. In the CA group, diffuse tumor cells were found in the bone marrow cavity of both femora.

This study presents a new mouse model of lung cancer bone metastasis with several advantages. Firstly, the establishment of bone metastases is fast and stable. The MLM system improved the local aggregation of cells in the femur, resulting in the appearance of precisely fixed tumor signals within 3 d after cell injection and these signals keep increasing over time. In contrast, the CA method only helped a small proportion of tumor cells reaching lower limbs through blood circulation. At +3 d, the tumor signal appeared randomly in one limb or both (sometimes neither) of lower limbs, and the intensity was significantly lower than that in the MLM group. Successful early modeling will effectively extend the therapeutic window of model mice, allowing for earlier intervention of the model, which is highly advantageous for new drug development and helps to explore the mechanisms of tumor development. Secondly, higher bone metastasis rate. As previously described, the bone metastasis rate in the CA group varied dynamically over 14 days (45.5–56.82%), whereas the rate in the MLM group remained stable at 82.76%. Thirdly, high consistency of bone metastasis. It is difficult to predict the exact location of bone metastasis and infiltration of vital organs in such modeling methods as CA, IC, IV, and IB injection, a wide variation in the frequency, signal intensity and location of tumor metastasis. In this study, tumor signals were observed in vital organs and at the femur, tibia, and knee joints in the CA group. While the MLM system enhanced the consistency of tumor modeling, in which tumor signals were limited to the femur with a consistent distribution, as well as significantly lower signals in vital organs at +14 d. In a word, the

MLM system increased the repeatability and reliability of tumor bone metastasis. It can be utilized for constructing other tumor types and patient-derived xenografts (PDX) models in the future.

4. Conclusion

Here, we show the biosafety and effect of A549-GL cells based MLM. It is the first report of tumor modeling with the MLM system to construct a precise tumor bone metastasis model. The manipulation of cells by the magnetic MLM system improves the precision of tumorigenic sites and bone metastasis rates, results in better consistency and repeatability of the model. This model has much longer study window for drug screening and treatment, as well as further mechanism study, due to its early and stable modeling and fewer infiltration of vital organs.

CRediT authorship contribution statement

Luxia Tang: Methodology. **Jinyan Luo:** Methodology. **Qiyan Chen:** Funding acquisition, Formal analysis, Data curation. **Jiawei Xu:** Writing – original draft. **Leyi Tan:** Project administration, Investigation. **Ning Gan:** Conceptualization. **Qiusui Mai:** Project administration, Investigation. **Xia Lu:** Project administration, Investigation. **Dingyi Zhang:** Writing – review & editing, Funding acquisition, Formal analysis. **Qianli Jiang:** Writing – original draft, Conceptualization. **Jialu Zhang:** Writing – original draft, Data curation, Conceptualization. **Zhengyuan Wang:** Validation.

Declaration of Competing Interest

The authors declare that they have no known competing financial interests or personal relationships that could have appeared to influence the work reported in this paper.

Data Availability

Data will be made available on request.

Acknowledgements

The authors thank Zhengshan Yi for flow cytometry assistance. The authors thank the students of Blood and Bone Marrow China—Xinyue Zhang, Yiming Zhao, Yufang Lv, Meilin Long, Lanlan Liang, Ye Xiao, Jianbin Liang, Lu Wang, Sian Zhang—who participated in this study with great enthusiasm. This work was supported by Natural Science Foundation of Guangdong Province (2016A030313585 and 2018A030313647); Science and Technology Planning Project of Guangdong Province (2018A070701006, 2020A1414050026); Science and Technology Program of Guangzhou (2024B03J0232); Undergraduate innovation and entrepreneurship training program (202312121030 and 202312121307).

Appendix A. Supporting information

Supplementary data associated with this article can be found in the online version at doi:10.1016/j.colsurfb.2024.113877.

References

[1] D. Santini, S. Barni, S. Intagliata, A. Falcone, F. Ferraù, D. Galetta, L. Moscetti, N. La Verde, T. Ibrahim, F. Petrelli, E. Vasile, L. Ginocchi, D. Ottaviani, F. Longo, C. Ortega, A. Russo, G. Badalamenti, E. Collovà, G. Lanzetta, G. Mansueto, V. Adamo, F. De Marinis, M.A. Satolli, F. Cantile, A. Mancuso, F.M. Tanca, R. Addeo, M. Russano, M. Sterpi, F. Pantano, B. Vincenzi, G. Tonini, Natural history of non-small-cell lung cancer with bone metastases, Sci. Rep. 5 (1) (2015), https://doi.org/10.1038/srep18670.

[2] A. Bongiovanni, F. Foca, J. Menis, S.L. Stucci, F. Artioli, V. Guadalupi, M. R. Forcignanò, M. Fantini, F. Recine, L. Mercatali, C. Spadazzi, M.A. Burgio, V. Fausti, A. Miserocchi, T. Ibrahim, Immune checkpoint inhibitors with or without bone-targeted therapy in nsclc patients with bone metastases and prognostic significance of neutrophil-to-lymphocyte ratio, Front. Immunol. 12 (2021), https://doi.org/10.3389/fimmu.2021.697298.

[3] P. Clézardin, R. Coleman, M. Puppo, P. Ottewell, E. Bonnelye, F. Paycha, C. B. Confavreux, I. Holen, Bone metastasis: mechanisms, therapies, and biomarkers, Physiol. Rev. 101 (3) (2021) 797–855, https://doi.org/10.1152/physrev.00012.2019.

[4] A. Camacho, S. Jerez, Bone metastasis treatment modeling via optimal control, J. Math. Biol. 78 (1-2) (2019) 497–526, https://doi.org/10.1007/s00285-018-1281-3.

[5] J. Fornetti, A.L. Welm, S.A. Stewart, Understanding the bone in cancer metastasis, J. Bone Miner. Res. 33 (12) (2018) 2099–2113, https://doi.org/10.1002/jbmr.3618.

[6] J.H. Tae, I.H. Chang, Animal models of bone metastatic prostate cancer, Investig. Clin. Urol. 64 (3) (2023) 219, https://doi.org/10.4111/icu.20230026.

[7] D. Lefley, F. Howard, F. Arshad, S. Bradbury, H. Brown, C. Tulotta, R. Eyre, D. Alférez, J.M. Wilkinson, I. Holen, R.B. Clarke, P. Ottewell, Development of clinically relevant in vivo metastasis models using human bone discs and breast cancer patient-derived xenografts, Breast Cancer Res 21 (1) (2019), https://doi.org/10.1186/s13058-019-1220-2.

[8] J.K. Simmons, B.E. Hildreth, W. Supsavhad, S.M. Elshafae, B.B. Hassan, W. P. Dirksen, R.E. Toribio, T.J. Rosol, Animal models of bone metastasis, Vet. Pathol. 52 (5) (2015) 827–841, https://doi.org/10.1177/0300985815586223.

[9] M. Elkin, I. Vlodavsky, Tail vein assay of cancer metastasis, Curr. Protoc. Cell Biol. Chapter 19 12 (2001) 19, https://doi.org/10.1002/0471143030.cb1902s12.

[10] M. Lelekakis, J.M. Moseley, T.J. Martin, D. Hards, E. Williams, P. Ho, D. Lowen, J. Javni, F.R. Miller, J. Slavin, R.L. Anderson, A novel orthotopic model of breast cancer metastasis to bone, Clin. Exp. Metastas-.-. 17 (2) (1999) 163–170, https://doi.org/10.1023/a:1006689719505.

[11] L.C. Bailey-Downs, J.E. Thorpe, B.C. Disch, A. Bastian, P.J. Hauser, T. Farasyn, W. L. Berry, R.E. Hurst, M.A. Ihnat, A. Angelucci, Development and characterization of a preclinical model of breast cancer lung micrometastatic to macrometastatic progression, Plos One 9 (5) (2014) e98624, https://doi.org/10.1371/journal.pone.0098624.

[12] B. Zhang, X. Li, W. Qian, D. Wu, J. Dong, Measurement of bone metastatic tumor growth by a tibial tumorigenesis assay, Bio-Protoc. 11 (22) (2021), https://doi.org/10.21769/BioProtoc.4231.

[13] Q. Mai, Z. Wang, Q. Chen, J. Zhang, D. Zhang, C. Li, Q. Jiang, Magnetically empowered bone marrow cells as a micro-living motor can improve early hematopoietic reconstitution, Cytotherapy 25 (2) (2023) 162–173, https://doi.org/10.1016/j.jcyt.2022.11.002.

[14] H.P. Farhoodi, A.I. Segaliny, Z.W. Wagoner, J.L. Cheng, L. Liu, W. Zhao, Optimization of a syngeneic murine model of bone metastasis, J. Bone Oncol. 23 (2020) 100298, https://doi.org/10.1016/j.jbo.2020.100298.

[15] T. Kuchimaru, N. Kataoka, K. Nakagawa, T. Isozaki, H. Miyabara, M. Minegishi, T. Kadonosono, S. Kizaka-Kondoh, A reliable murine model of bone metastasis by injecting cancer cells through caudal arteries, Nat. Commun. 9 (1) (2018), https://doi.org/10.1038/s41467-018-05366-3.

[16] Z. Huang, Y. Shen, A. Sun, G. Huang, H. Zhu, B. Huang, J. Xu, Y. Song, N. Pei, J. Ma, X. Yang, Y. Zou, J. Qian, J. Ge, Magnetic targeting enhances retrograde cell retention in a rat model of myocardial infarction, Stem Cell Res. Ther. 4 (6) (2013) 149, https://doi.org/10.1186/scrt360.

[17] W. Yun, J. Choi, H. Ju, M. Kim, S. Choi, E. Oh, Y. Seo, J. Key, Enhanced homing technique of mesenchymal stem cells using iron oxide nanoparticles by magnetic attraction in olfactory-injured mouse models, Int. J. Mol. Sci. 19 (5) (2018) 1376, https://doi.org/10.3390/ijms19051376.

[18] R.A. Burga, D.H. Khan, N. Agrawal, C.M. Bollard, R. Fernandes, Designing magnetically responsive biohybrids composed of cord blood-derived natural killer cells and iron oxide nanoparticles, Bioconj. Chem. 30 (3) (2019) 552–560, https://doi.org/10.1021/acs.bioconjchem.9b00048.

[19] K. Kim, J. Han, S.H. Choi, H. Jung, J.D. Park, H. An, S. Kim, D. Kim, J. Doh, D. K. Han, I. Kim, W. Park, K. Park, Cationic nanoparticle-mediated activation of natural killer cells for effective cancer immunotherapy, ACS Appl. Mater. Interfaces 12 (51) (2020) 56731–56740, https://doi.org/10.1021/acsami.0c16357.

[20] Y. Alapan, O. Yasa, O. Schauer, J. Giltinan, A.F. Tabak, V. Sourjik, M. Sitti, Soft erythrocyte-based bacterial microswimmers for cargo delivery, Sci. Robot. 3 (17) (2018), https://doi.org/10.1126/scirobotics.aar4423.

[21] L. Kiru, A. Zlitni, A.M. Tousley, G.N. Dalton, W. Wu, F. Lafortune, A. Liu, K. M. Cunanan, H. Nejadnik, T. Sulchek, M.E. Moseley, R.G. Majzner, H.E. Daldrup-Link, In vivo imaging of nanoparticle-labeled car t cells, Proc. Natl. Acad. Sci. 119 (6) (2022), https://doi.org/10.1073/pnas.2102363119.

[22] X. Wang, J. Cai, L. Sun, S. Zhang, D. Gong, X. Li, S. Yue, L. Feng, D. Zhang, Facile fabrication of magnetic microrobots based onspirulina templates for targeted delivery and synergistic chemo-photothermal therapy, ACS Appl. Mater. Interfaces 11 (5) (2019) 4745–4756, https://doi.org/10.1021/acsami.8b15586.

[23] H. Mu, C. Liu, Q. Zhang, H. Meng, S. Yu, K. Zeng, J. Han, X. Jin, S. Shi, P. Yu, T. Li, J. Xu, Y. Hua, Magnetic-driven hydrogel microrobots selectively enhance synthetic lethality in mtap-deleted osteosarcoma, Front. Bioeng. Biotechnol. 10 (2022), https://doi.org/10.3389/fbioe.2022.911455.

[24] H.Y. Zhang, Z.S. Li, C.Y. Gao, X.J. Fan, Y.X. Pang, T.L. Li, Z.G. Wu, H. Xie, Q. He, Dual-responsive biohybrid neutrobots for active target delivery, Sci. Robot. 6 (52) (2021), https://doi.org/10.1126/scirobotics.aaz9519.

[25] D. Son, H. Gilbert, M. Sitti, Magnetically actuated soft capsule endoscope for fine-needle biopsy, Soft Robot 7 (1) (2020) 10–21, https://doi.org/10.1089/soro.2018.0171.

[26] C. Lv, Y. Yang, B. Li, Nano/micromotors in active matter, Micromachines 13 (2) (2022) 307, https://doi.org/10.3390/mi13020307.
[27] T. Gwisai, N. Mirkhani, M.G. Christiansen, T.T. Nguyen, V. Ling, S. Schuerle, Magnetic torque-driven living microrobots for enhanced tumor infiltration, Cold Spring Harbor Laboratory Press, Cold Spring Harbor, ⟨https://doi.org/10.1101/2022.01.03.473989⟩.
[28] M.B. Akolpoglu, Y. Alapan, N.O. Dogan, S.F. Baltaci, O. Yasa, T.G. Aybar, M. Sitti, Magnetically steerable bacterial microrobots moving in 3d biological matrices for stimuli-responsive cargo delivery, Sci. Adv. 8 (28) (2022) o6163, https://doi.org/10.1126/sciadv.abo6163.
[29] Y. Alapan, U. Bozuyuk, P. Erkoc, A.C. Karacakol, M. Sitti, Multifunctional surface microrollers for targeted cargo delivery in physiological blood flow, Sci. Robot. 5 (42) (2020), https://doi.org/10.1126/scirobotics.aba5726.
[30] V. Sridhar, F. Podjaski, Y. Alapan, J. Kröger, L. Grunenberg, V. Kishore, B. V. Lotsch, M. Sitti, Light-driven carbon nitride microswimmers with propulsion in biological and ionic media and responsive on-demand drug delivery, Sci. Robot. 7 (62) (2022), https://doi.org/10.1126/scirobotics.abm1421.
[31] A. Aghakhani, O. Yasa, P. Wrede, M. Sitti, Acoustically powered surface-slipping mobile microrobots, Proc. Natl. Acad. Sci. U. S. A. 117 (7) (2020) 3469–3477, https://doi.org/10.1073/pnas.1920099117.
[32] J.F. Louf, N. Bertin, B. Dollet, O. Stephan, P. Marmottant, Hovering microswimmers exhibit ultrafast motion to navigate under acoustic forces, Adv. Mater. Interfaces 5 (16) (2018) 1800425, https://doi.org/10.1002/admi.201800425.
[33] G. Loget, A. Kuhn, Electric field-induced chemical locomotion of conducting objects, Nat. Commun. 2 (1) (2011), https://doi.org/10.1038/ncomms1550.
[34] E.E. Niedert, C. Bi, G. Adam, E. Lambert, L. Solorio, C.J. Goergen, D.J. Cappelleri, A tumbling magnetic microrobot system for biomedical applications, Micromachines 11 (9) (2020) 861, https://doi.org/10.3390/mi11090861.
[35] A. Farzin, S.A. Etesami, J. Quint, A. Memic, A. Tamayol, Magnetic nanoparticles in cancer therapy and diagnosis, Adv. Healthc. Mater. 9 (9) (2020) 1901058, https://doi.org/10.1002/adhm.201901058.
[36] I.M. El-Sherbiny, N.M. Elbaz, M. Sedki, A. Elgammal, M.H. Yacoub, Magnetic nanoparticles-based drug and gene delivery systems for the treatment of pulmonary diseases, Nanomedicine 12 (4) (2017) 387–402, https://doi.org/10.2217/nnm-2016-0341.
[37] Y. Wang, S. Zhou, R. Yang, M. Rahman, R.C. Sequeira, N. Cao, Y. Zhang, W. Zhao, Q. Fu, Magnetic targeting of super-paramagnetic iron oxide nanoparticle labeled myogenic-induced adipose-derived stem cells in a rat model of stress urinary incontinence, Nanomed.: Nanotechnol., Biol. Med. 30 (2020) 102281, https://doi.org/10.1016/j.nano.2020.102281.
[38] F.Q. Hour, A.J. Moghadam, A. Shakeri-Zadeh, M. Bakhtiyari, R. Shabani, M. Mehdizadeh, Magnetic targeted delivery of the spions-labeled mesenchymal stem cells derived from human wharton's jelly in alzheimer's rat models, J. Control. Release 321 (2020) 430–441, https://doi.org/10.1016/j.jconrel.2020.02.035.
[39] C.C. Chang, J.Y. Tseng, D.R. Ji, C.Y. Chiu, D.S. Lu, C.Y. Chang, M.H. Yuan, C. F. Chang, C.S. Chiou, Y.H. Chen, J.L. Shie, Adsorption removal of environmental hormones of dimethyl phthalate using novel magnetic adsorbent, ScientificWorldJournal 2015 (2015) 903706, https://doi.org/10.1155/2015/903706.
[40] T. Zeng, X. Zhang, H. Niu, Y. Ma, W. Li, Y. Cai, In situ growth of gold nanoparticles onto polydopamine-encapsulated magnetic microspheres for catalytic reduction of nitrobenzene, Appl. Catal. B: Environ. 134-135 (2013) 26–33, https://doi.org/10.1016/j.apcatb.2012.12.037.
[41] J. Dai, J. Hensel, N. Wang, M. Kruithof-De Julio, Y. Shiozawa, Mouse models for studying prostate cancer bone metastasis, Bone Rep. 5 (2016), https://doi.org/10.1038/bonekey.2016.4.
[42] L. Yu-Lee, G. Yu, Y. Lee, S. Lin, J. Pan, T. Pan, K. Yu, B. Liu, C.J. Creighton, J. Rodriguez-Canales, P.A. Villalobos, I.I. Wistuba, E. de Nadal, F. Posas, G. E. Gallick, S. Lin, Osteoblast-secreted factors mediate dormancy of metastatic prostate cancer in the bone via activation of the tgfβriii–p38mapk–ps249/t252rb pathway, Cancer Res 78 (11) (2018) 2911–2924, https://doi.org/10.1158/0008-5472.CAN-17-1051.
[43] M.A. Lawson, M.M. Mcdonald, N. Kovacic, W. Hua Khoo, R.L. Terry, J. Down, W. Kaplan, J. Paton-Hough, C. Fellows, J.A. Pettitt, T. Neil Dear, E. Van Valckenborgh, P.A. Baldock, M.J. Rogers, C.L. Eaton, K. Vanderkerken, A.R. Pettit, J.M.W. Quinn, A.C.W. Zannettino, T.G. Phan, P.I. Croucher, Osteoclasts control reactivation of dormant myeloma cells by remodelling the endosteal niche, Nat. Commun. 6 (1) (2015), https://doi.org/10.1038/ncomms9983.
[44] R. Dai, M. Liu, X. Xiang, Z. Xi, H. Xu, Osteoblasts and osteoclasts: an important switch of tumour cell dormancy during bone metastasis, J. Exp. Clin. Cancer Res. 41 (1) (2022), https://doi.org/10.1186/s13046-022-02520-0.